# Structure and Formation Mechanism of Black TiO₂ Nanoparticles

Mengkun Tian,[†] Masoud Mahjouri-Samani,[‡] Gyula Eres,[*,§] Ritesh Sachan,[§] Mina Yoon,[‡] Matthew F. Chisholm,[§] Kai Wang,[‡] Alexander A. Puretzky,[‡] Christopher M. Rouleau,[‡] David B. Geohegan,[‡] and Gerd Duscher[*,†,§]

[†]Department of Materials Science and Engineering, University of Tennessee, Knoxville, Tennessee 37996, United States and [‡]Center for Nanophase Materials Sciences and [§]Materials Science and Technology Division, Oak Ridge National Laboratory, Oak Ridge, Tennessee 37831, United States

ABSTRACT The remarkable properties of black TiO₂ are due to its disordered surface shell surrounding a crystalline core. However, the chemical composition and the atomic and electronic structure of the disordered shell and its relationship to the core remain poorly understood. Using advanced transmission electron microscopy methods, we show that the outermost layer of black TiO₂ nanoparticles consists of a disordered Ti₂O₃ shell. The measurements show a transition region that connects the disordered Ti₂O₃ shell to

the perfect rutile core consisting first of four to five monolayers of defective rutile, containing clearly visible Ti interstitial atoms, followed by an ordered reconstruction layer of Ti interstitial atoms. Our data suggest that this reconstructed layer presents a template on which the disordered Ti₂O₃ layers form by interstitial diffusion of Ti ions. In contrast to recent reports that attribute TiO₂ band-gap narrowing to the synergistic action of oxygen vacancies and surface disorder of nonspecific origin, our results point to Ti₂O₃, which is a narrow-band-gap semiconductor. As a stoichiometric compound of the lower oxidation state Ti^{3+} it is expected to be a more robust atomic structure than oxygen-deficient TiO₂ for preserving and stabilizing Ti^{3+} surface species that are the key to the enhanced photocatalytic activity of black TiO₂.
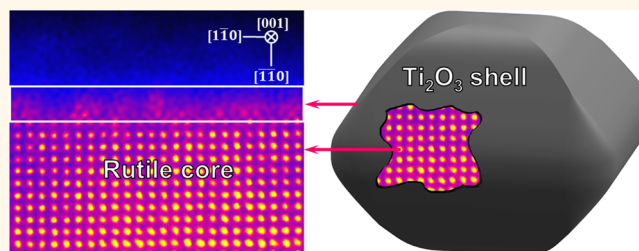
Nanoparticles (NPs) of TiO₂ are of great interest because they present a platform for creating unique nanostructures with properties that do not exist in bulk phases.[1] The best known such nanostructures are quantum dots (QDs), the properties of which are governed purely by spatial confinement of the bulk phase achieved by tuning the particle size.[2] A particularly intriguing NP structure that became broadly known as black TiO₂ consists of a perfectly crystalline core and a 1−2 nm thick disordered shell.[3−5] The significance of black TiO₂ is that it exhibits dramatically higher photocatalytic activity than ordinary white TiO₂ NPs. In contrast to QDs the properties of black TiO₂ NPs are primarily related to a thin disordered surface layer characterized by the disruption of the bulk periodicity. It has been shown empirically that the formation of structural imperfections that govern these properties is highly sensitive to the synthesis methods.[5] It is believed that the common factors in all black TiO₂ independent of the method of formation are the oxygen vacancies and surface disorder.[6] The band-gap narrowing that is central to enhance photocatalytic activity of black TiO₂ is attributed to a synergistic action between oxygen vacancies and structural defects in the disordered layer.[4] It is argued that black TiO₂ is uniquely stable because the metastable disordered phase is frozen in. It is shown that reducing crystalline, white TiO₂ powders (Degussa P25) produces only pale blue samples with no red shift in the absorption spectra.[4] However, because of the scarcity of methods capable of probing isolated NPs, the chemical composition of the disordered layer and how the atomic and electronic structure are linked together in band-gap narrowing of black TiO₂ remain intensely debated.

In this work we use state-of-the-art transmission electron microscopy (TEM) methods including monochromated electron energy-loss spectroscopy (EELS), fifth-order

aberration-corrected scanning transmission electron microscopy (STEM), and nanobeam electron diffraction (NBED) to construct a picture of black TiO_2 on a single-particle level. The black TiO_2 NPs were formed by a novel method using crystallization of amorphous ultra-small nanoparticles (UNPs) synthesized by pulsed laser vaporization (PLV). It is important for understanding the formation and structure of black TiO_2 that the disordered layer forms only if crystallization is performed in an oxygen-free environment. We used pure Ar at 970 ± 20 K. The objective of this work was to determine the chemical composition and the atomic and electronic structure of the disordered shell and its relationship to the crystalline core in black TiO_2. The electronic structure was measured by EELS as a function of depth from the surface to determine the phase and the formation of defects from broadening of the characteristics EELS features of Ti oxides. The key result from EELS is that the core consists of perfectly crystalline rutile and the disordered outermost layers consist of Ti_2O_3, the stoichiometric form of the lower oxidation state Ti^{3+}. However, EELS also reveals that between the core and the shell there is a transition region that could not be unambiguously determined because of the severely increasing broadening of the EELS features as the surface is approached. The sequence of these defective layers and their structure were determined using atomic-resolution high-angle annular dark-field (HAADF) imaging. Two types of defective layers both containing interstitial Ti atoms were identified. We propose a mechanism that shows that both types of interstitial layers are critical in the formation of the outermost disordered Ti_2O_3 shell.

The enhanced photocatalytic activity in black TiO_2 produced by various implementations of hydrogen reduction including direct crystallization in a hydrogen stream[4] is typically attributed to a combination of lattice disorder near the surface layer and the presence of chemical species such as oxygen vacancies, Ti^{3+} ions, and Ti−OH and Ti−H groups.[1] Our results from crystallization in pure Ar point to Ti_2O_3, a stable stoichiometric compound of the lower oxidation state of Ti^{3+}, as the main component of the disordered layer. The distinction is important on two levels. First, Ti_2O_3 is intrinsically a narrow-band-gap semiconductor, needing no extrinsic mechanisms such as doping for increasing the solar energy absorption efficiency. Second, as a stoichiometric compound, it is likely to be more robust in preserving the stability of Ti^{3+} species than the various metastable defective TiO_2 phases formed by hydrogen reduction and similar methods.

RESULTS AND DISCUSSION

The high-resolution TEM (HRTEM) image in Figure 1a shows room-temperature PLV-produced aggregates of TiO_2 UNPs of clearly identifiable shape that are typically smaller than 5 nm. On the basis of selected-area electron
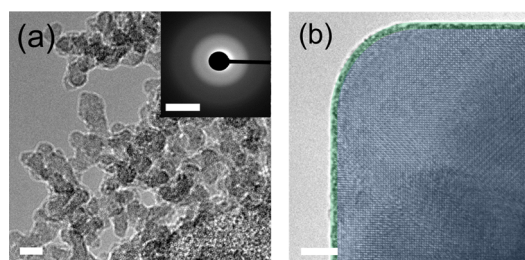

Figure 1. High-resolution TEM images of TiO_2 nanoparticles. (a) HRTEM image of UNP aggregates synthesized by PLV at room temperature. The inset is a SAED pattern that indicates that these UNPs are amorphous. Scale bar in the inset is 5/nm. (b) HRTEM image of a crystalline particle viewed in the [001] zone axis showing the core (blue) and a disordered shell (green line). Scale bars are 5 nm.

diffraction (SAED) data that in the inset of Figure 1a show no periodicity, we conclude that the UNPs are amorphous. The first important result of this work is that after annealing in pure Ar for 2 h at 970 ± 20 K the amorphous UNPs crystallize into larger dark particles with the diameter of 90% of the NPs exceeding 15 ± 1 nm, as shown in Figure 1b.

We use several local electron microscopy (EM) techniques to determine the structure and the composition of these black TiO_2 NPs. The high-resolution TEM image in Figure 1b clearly shows a nanocrystalline core that is surrounded by a thin disordered shell. The characteristic features of the energy-loss near-edge structure (ELNES) illustrated in Figure 2a and d are used to identify various Ti oxides in differentiating the core from the shell and determining the composition of the disordered shell. The first two peaks in the ELNES comparing the O-K edge of Ti oxides in Figure 2a designated by a and b correspond to the transition from O-1s state to the energy levels originating from O-2p hybridized with Ti t_{2g} and e_g orbitals. The intensity reversal of these two peaks from a < b for Ti_2O_3 to a > b for rutile serves to uniquely differentiate the rutile core from the Ti_2O_3[7,8] shell as a function of distance from the surface.

Following the unique identification of the core and the shell, the changing composition of the shell as a function of depth is determined by linear least-squares fitting using the reference spectra for Ti_2O_3 and rutile O-K edge shown in Figure 2a. The excellent fits in Figure 2b and c, within the noise limit determined from the pre-edge region, demonstrate that all the spectral features of the line scans at different depths shown in Figure 2g can be faithfully reproduced by a linear combination of the Ti_2O_3 and the rutile spectra. The excellent agreement validates the use of this linear least-squares fitting approach for quantitative determination of the fraction of Ti_2O_3 from the experimental spectra. Further details of the fitting method are illustrated in Figures S1 and S2. The plot in Figure 2g derived from the overall fits shows that the increase in the Ti_2O_3 fraction approaching the surface coincides with the reversal of the intensity pattern of the a and b
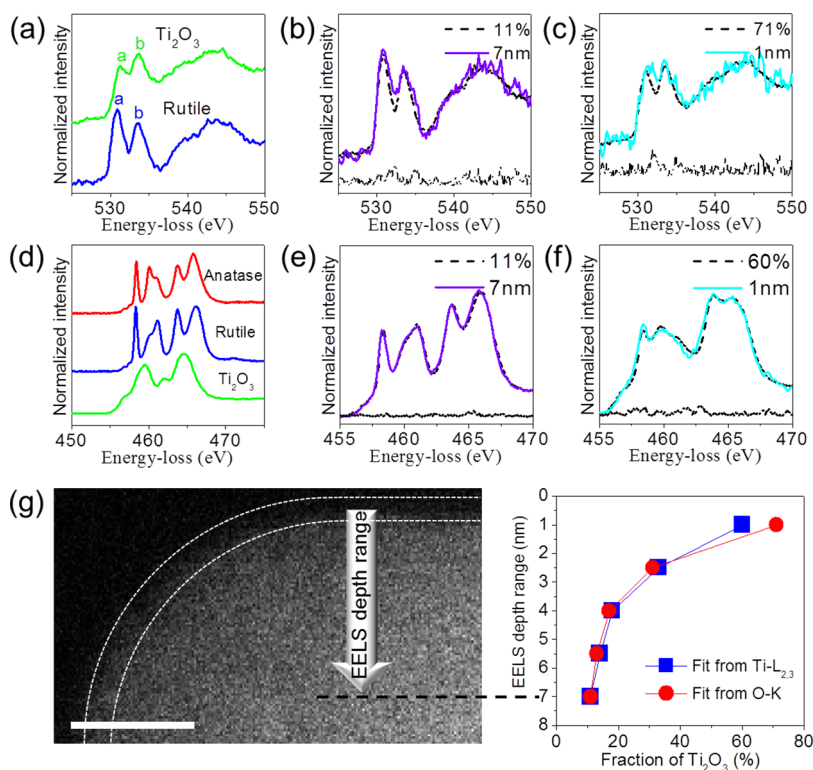
Figure 2. EELS characterization of the rutile NP in Figure 1b as a function of surface depth. The origins of the reference titanium oxide spectra are described in the Supporting Information. (a) Reference spectra of the O-K edge of Ti_2O_3 NPs and rutile NPs, showing that the intensity pattern of the a and b peaks is uniquely different. (b, c) Experimental EELS spectra of the O-K edge at different depths from the surface of a rutile NP compared with fits from a linear combination of the reference rutile and Ti_2O_3 spectra. The coefficients are determined by linear least-squares fitting, representing the fractions of Ti_2O_3 of 11% and 71% at locations 7 and 1 nm away from the vacuum, respectively. The residuals of the linear least-squares fitting are given at the bottom of each plot. (d) Comparison of the spectral features in $Ti-L_{2,3}$ ELNES of pure anatase, rutile, and Ti_2O_3, all of which are in NP forms. (e, f) $Ti-L_{2,3}$ part of the experimental EELS spectra at 7 and 1 nm from the surface of the rutile NPs compared with fits from a linear combination of the reference rutile and Ti_2O_3 spectra. The fraction of Ti_2O_3 is 11% for 7 nm and 60% for 1 nm, respectively. The residuals of the linear least-squares fitting are given at the bottom of each plot. (g) TEM image on the NP edge region (left) and plot of Ti_2O_3 fractions as a function of distance from the vacuum (right) obtained by fitting the $Ti-L_{2,3}$ and O-K edge spectra. Scale bar is 5 nm.

peaks in the O-K edge, which is largely completed within the outer 1 nm of the particles, as shown in Figure 2d.

The analysis and the fitting of the O-K edges have clearly identified Ti_2O_3 as the main factor responsible for the broadening and blurring of the EELS spectral features. With this in mind we extend the linear least-squares fitting procedure to perform the same analysis using the $Ti-L_{2,3}$ edge data, which were acquired simultaneously with the O-K edge. Figure 2d shows that the ELNES of $Ti-L_{2,3}$ edge exhibits more distinct features than the O-K edge and facilitates further differentiation of the TiO_2 phases. Both pure anatase and rutile in Figure 2d exhibit two groups of peaks associated with transitions from 2p core electrons to the t_{2g} and e_g sub-bands in the conduction band. With the high-energy resolution of monochromated EELS, one can easily distinguish anatase from rutile by the inverted "shoulder" of the L_3-e_g peaks in the EELS spectra. In contrast, the ELNES of Ti_2O_3 shows quite different crystal field splitting features in two broad peaks and two small prepeaks, related to a

different connectivity and distortion of the TiO_6 octahedral units.[7]

The $Ti-L_{2,3}$ edge data in Figure 2e and f also confirm rutile as the phase of the core of the NPs and an increasing Ti_2O_3 fraction in the near surface region. Similar to the O-K edge, we fit the experimental spectra to a linear combination of Ti_2O_3 and rutile reference spectra. The data and spectral fit for each thickness data point of the plot in Figure 2g are given in Figure S2. With the exception of the spectrum taken 1 nm away from surface, the fractions of Ti_2O_3 derived from the two independent least-squares fits of the $Ti-L_{2,3}$ edge and the O-K edge agree within 2% error. The larger error (~10%) in the 1 nm fit is attributed to a poor signal-to-noise ratio in the weaker O-K edge signal, as shown in Figure 2g. Consistent with the O-K edge data, this fit reveals a constant but small contribution of Ti_2O_3 to the $Ti-L_{2,3}$ ELNES of the NP interior 4 to 7 nm away from the vacuum (surface). The apparent Ti_2O_3 component of the core signal is contributed by the surface layer, and it is a detection geometry effect discussed further in the Supporting Information and Figure S3.
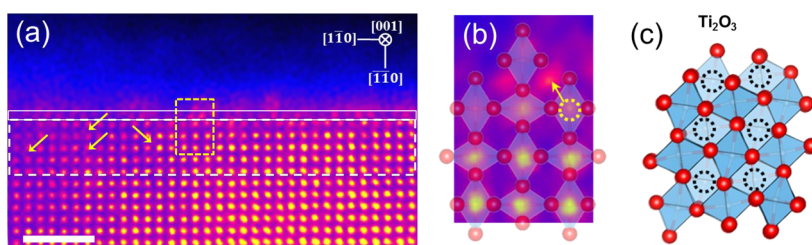
Figure 3. Atomic-resolution high-angle annular dark-field (HAADF) image of a rutile NP viewed in the [001] direction and crystal structure models of connected TiO_6 octahedra for rutile and Ti_2O_3. This rutile NP comes from the same sample as the one in Figure 2. (a) HAADF image of a rutile NP viewed in the [001] direction. The surface reconstruction layer consisting of an ordered line of interstitial Ti atoms is located above the rutile {110} plane designated by a solid white rectangle. The disordered Ti_2O_3 layers form on top of the surface reconstruction layer. The yellow arrows designate a few Ti atoms near the surface that are displaced from the rutile basis in a series of defective rutile layers designated by a dashed white rectangle. (b) Magnified image from the area highlighted by the dashed yellow rectangle in (a) and compared with the corundum Ti_2O_3 structure on the right. (c) The Ti atoms in the light blue octahedra in corundum Ti_2O_3 originate from the diffusion of interstitial Ti atoms in rutile, associated with a unit cell distortion. Scale bar is 2 nm.

Figure 2g shows that at 1 nm from the surface the fraction of Ti_2O_3 dramatically jumps by more than a factor of 5. Assuming that after neglecting the small surface contributions (∼10%) the core EELS spectra represent white TiO_2, the comparison between the EELS spectra in Figure 2b and c for the O-K edge and Figure 2e and f for the Ti-$L_{2,3}$ edge reveals the EELS features that unambiguously differentiate white TiO_2 from black TiO_2. In addition, comparison of the spectra in Figure 2e and f shows the rutile intensity maxima associated with the L_3 edge features becoming inverted, which now surprisingly resembles a smeared out anatase signal. Closer examination of the spectra in Figure 2d reveals that this intensity reversal is caused by the large contribution from the first Ti_2O_3 edge to the rutile intensity maxima. The blurring of spectral features is indicative of the structural changes of the NPs associated with increasing Ti_2O_3 concentration in the near surface region, indicating that the inverted shoulder of L_3-e_g peaks alone is no longer sufficient for identifying the TiO_2 phases in the surface region.

Since we are characterizing single NP, it is important to note that the NP size plays a critical role in the analysis of the core—shell effects. In addition to the increased compositional broadening by the Ti_2O_3 shell, an extra broadening component in smaller NPs may arise from structural defects and disorder that do not have a known or specific EELS spectral signature. To complement the EELS data and explore the structure of the defective layers in the region between the core and the Ti_2O_3 shell, we use atomic-resolution STEM to image directly the surface structure of the rutile NPs viewed parallel to the surface in the [001] direction. The image in Figure 3a shows atomically rough surface layers of nonuniform thickness exhibiting a periodicity different from rutile. This STEM image was taken from a rutile NP in the same sample as the one in Figure 2. The atomically rough surface and irregular periodicity of the top layers indicate that the outer shell is highly defective. Below the outermost layers are several defective rutile layers, highlighted by a white dashed

rectangle, containing interstitial Ti atoms displaced from the rutile basis marked by yellow arrows. The periodicity in the subsequent layers corresponds to that of perfect rutile, consistent with the least-squares fitting of EELS spectra in Figure 2g. However, the atomic positions of Ti in the first layer on top of the defective rutile layers designated by a faint solid white rectangle have a periodicity clearly different from that of rutile. This structure is in good agreement with the report by Shibata et al.,[9] who observed a single reconstruction layer of interstitial Ti atoms above the (110) surface by directly imaging the reduced surface of a rutile thin film using atomic-resolution STEM. This reconstruction layer,[10] whose symmetry is commonly accepted as "added row Ti_2O_3",[11,12] can be routinely observed after thermal annealing in a vacuum.
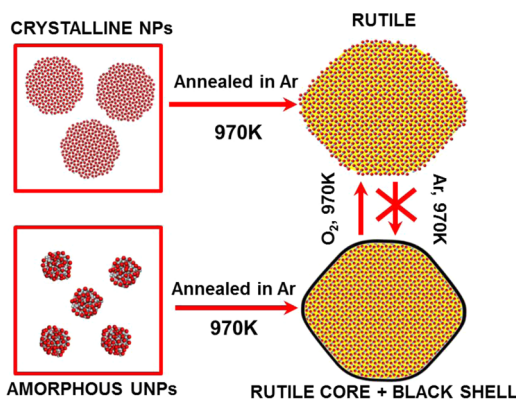
In this work we show that Ti_2O_3 growth occurs on this reconstruction layer. Stone et al.[13] reported that when annealed in an O_2 atmosphere a stoichiometric TiO_2 regrows above the rutile (110) plane on these surface reconstruction layers. The stoichiometric surface layers form by reoxidation of Ti^{n+} interstitials migrating from the interior of the particle. We rule out this mechanism because our background ambient is O_2 deficient. The formation of Ti_2O_3 by a topotactic reduction of rutile that occurs by the diffusion of Ti^{3+} ions into the interstitial site of rutile discussed by Tominaka[14] provides a more plausible mechanism. According to their picture illustrated in Figure 3b, the TiO_2—Ti_2O_3 phase transformation is initiated by interstitial diffusion of nearby Ti ions from the light blue TiO_6 octahedra to the interstitial sites in rutile. The Ti^{3+} ions are formed as a result of charge compensation associated with oxygen vacancy formation. The STEM image shows that the rutile structure combining with the "extra" Ti atoms in the surface reconstruction layer, or the interstitial Ti atoms below this layer, in general matches the crystal structure of corundum Ti_2O_3 in the [001] projection direction, illustrated in Figure 3c. The bulk segments in Figure 3b and c illustrate the transformation of the connectivity of TiO_6 octahedral units
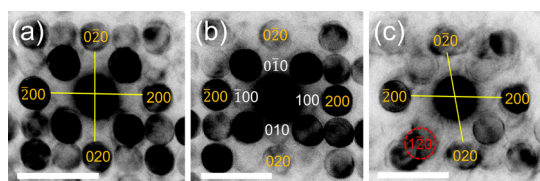
Figure 4. Representative NBED patterns of the core—shell TiO$_2$ NP from the same one in Figure 2. (a) NBED pattern of the core 2—4 nm away from vacuum of the rutile NP showing perfect rutile symmetry. (b) NBED pattern of the near surface area showing the appearance of reflections forbidden in rutile designated by the white indices. (c) The NBED pattern of the surface area shows deviations from a standard rutile diffraction pattern in the rotation of the (020) and (0$\bar{2}$0) reflections. An example of extra reflections marked by the red circle is attributed to defective Ti$_2$O$_3$. Scale bars are 5/nm.

Figure 5. Schematic illustration of the steps in black TiO$_2$ core—shell nanoparticle formation and conversion. Both crystalline NPs and amorphous UNPs agglomerate into larger particles when annealed in Ar. However, only the amorphous TiO$_2$ UNPs result in formation of a Ti$_2$O$_3$ shell characteristic of black TiO$_2$. Annealing of black TiO$_2$ in O$_2$ at 970 $\pm$ 20 K forms ordinary white rutile NPs. This process cannot be reversed to obtain black TiO$_2$ by repeating the annealing in Ar.

from edge and corner shared in rutile to face and edge shared in Ti$_2$O$_3$.[15] The change in octahedral connectivity is accompanied by a distortion of the octahedral units creating lattice distortions at the interface. The lattice mismatch becomes even larger if Ti$_2$O$_3$ grows on rutile planes other than {110}. Considering that the surface of the NPs is not a single well-defined crystal plane, growth of Ti$_2$O$_3$ on different crystal planes of rutile is expected to cause severe lattice distortions, resulting in Ti$_2$O$_3$ with highly disordered crystal structure. A beneficial effect of larger lattice strain is an increase in conductivity. According to the Goodenough model, the Ti$_2$O$_3$ semiconductor band-gap becomes narrower with increasing the c/a ratio of lattice constants.[16]

We use NBED to provide further structural details of the core—shell relationship in the same black TiO$_2$ NP in Figure 2. The NBED pattern of the core in Figure 4a exhibits 4-fold symmetry, designated by the yellow bars, characteristic of pure rutile, with minor contributions from the Ti$_2$O$_3$ shell and lattice distortions. As the surface is approached, new reflections both kinetically and dynamically forbidden in pure rutile ({100} in the [001] zone axis) appear 2 to 4 nm away from the vacuum shown in Figure 4b. The existence of these forbidden reflections indicates a deviation of Ti atoms from octahedral symmetry.[17] These forbidden reflections indicate that the Ti atoms suffered a distortion by traces of oxygen vacancies[18] as they were expelled toward the surface during the crystallization of the core. This interpretation is consistent with the displacement of Ti atoms at the same depth, designated by yellow arrows in the STEM image. Some contribution by low-intensity forbidden reflections originating from the top and bottom surface regions of the NPs may also be observed in NBED patterns of the interior of the particle. The NBED pattern from the shell region in Figure 4c corresponds to a highly defective crystalline structure with geometrically suppressed intensity. To probe the surface area, we slightly defocus the beam to increase the probe size to 1—2 nm and thus reduce the disturbance from roughness and sample drift. The NBED patterns from this location contain the structural information on both the rutile core and the shell. A significant distortion of the rutile structure is apparent in Figure 4c, which originates from the increased concentration of oxygen vacancies in the surface region of rutile. These distortions are represented by a rotation of the (020) and (0$\bar{2}$0) reflections, resulting in the loss of the 4-fold symmetry. A representative example of extra reflections of varying intensity marked by the red circle is attributed to the defective shell with a *d*-spacing close to that in Ti$_2$O$_3$ ($\bar{1}$20). The highly defective crystallinity of the surface layer and the off-zone axis viewing direction prevent us from mapping out the full symmetry of Ti$_2$O$_3$ by NBED. However, the depth-dependent structural details of the core—shell NPs obtained by NBED are highly consistent with the STEM image and complement the EELS spectral fits.

We attribute the unique surface structure of the black rutile NPs to crystallization of the amorphous UNPs in an oxygen-deficient environment maintained by the pure Ar atmosphere. The main steps in black TiO$_2$ NP formation illustrated in Figure 5 are deduced from the EM data. The first step in this process is the formation of amorphous UNPs by PLV. The capability to control the NPs' size, crystallinity, and oxygen stoichiometry during synthesis is a distinct advantage that PLV has over conventional methods such as sol—gel.[1] The UNPs for this work were synthesized in 200 mTorr of pure O$_2$, which is known to produce stoichiometric TiO$_2$. Annealing of these amorphous UNPs in Ar at 970 $\pm$ 20 K sets up a dynamic oxygen deficiency gradient during crystallization. The observation of the stoichiometric rutile core by EELS, STEM, and NBED measurements suggests that the starting point of this

gradient is at the core of the NPs. Oxygen vacancies, which are the primary defects in partially oxidized TiO_2,[19] accumulate and propagate toward the surface region during crystallization, creating an effective composition gradient, with increasing oxygen deficiency reaching a maximum at the surface of the NPs. When the concentration of oxygen vacancies reaches a saturation level beyond which the TiO_2 structure is no longer sustainable, Ti_2O_3, the stoichiometric phase of Ti^{3+}, forms on the outermost surface. The formation of Ti_2O_3 is not arbitrary. It is dictated by the structural relationship between the increasingly oxygen deficient rutile layers forming on top of the rutile surface. The defective Ti_2O_3 layer forms on the transition layer by interstitial diffusion of Ti ions from the defective rutile to the interface region, as shown in Figure 3b.

We test the hypothesis that the amorphous precursor is the key to the formation of the Ti_2O_3 surface shell by performing the annealing of the NPs in Ar and O_2 backgrounds. The black rutile NPs form after annealing of amorphous UNPs in Ar at 970 ± 20 K for 1 h, as shown in Figure S4. If the amorphous UNPs are annealed in air at the same temperature and time duration, white rutile NPs form. Additionally, initially black rutile NPs turn into the characteristic white color TiO_2 rutile NPs after annealing in air at the same temperature and time duration. However, the color change is not reversible. When the white rutile NPs are annealed in Ar at 970 ± 20 K, they remain white, indicating that the NP surface remains stable as crystalline rutile. According to first-principles density functional theory calculations that we performed to model the $TiO_2-Ti_2O_3$ phase transformation, Figure S5 shows that the crystalline rutile core forms at high oxygen partial pressure and changes to Ti_2O_3 with falling oxygen partial pressure. The fact that the reverse phase transformation is not observed in practice points to a possible kinetic barrier that prevents the transformation of rutile to Ti_2O_3 at this temperature. The effects of this kinetic barrier were also confirmed by performing EELS control experiments using stoichiometric crystalline rutile NPs (Degussa P25). Annealing in pure Ar at

970 ± 20 K shows no observable changes in Ti-$L_{2,3}$ ELNES in Figure S6. We conclude that the amorphous precursors play a unique role in the formation of a Ti_2O_3 disordered shell on a crystalline core that cannot be obtained simply by annealing of crystalline rutile NPs in pure Ar.

CONCLUSION

In summary, we used advanced TEM methods to construct a single-particle-level picture of the disordered shell and its coupling to the crystalline core in black TiO_2. The key result is that the outermost layer of the disordered shell consists of Ti_2O_3, a stoichiometric phase of the lower oxidation state Ti^{3+}. The Ti_2O_3 shell is connected to the crystalline rutile core by a transition region that consists of several monolayers of defective rutile, containing interstitial Ti atoms that are capped off by a single reconstructed monolayer of ordered interstitial Ti atoms. We show that the sequence of these defective layers plays a critical role in the formation of the Ti_2O_3 outermost disordered layer by interstitial diffusion of Ti^{3+} ions to the surface. The specific relationship between the sequence of defective layers and the crystalline core leads to the general conclusion that the structure of black TiO_2 is not totally arbitrary. The degree of "blackness" of TiO_2 structures is governed by the structural relationship between the type and sequence of oxygen-deficient layers that are formed as a function of the strength of the reducing background during formation. The sensitivity of the properties of black TiO_2 to the synthesis methods is a direct manifestation of the changing strength of the reducing background on the electronic structure measured here by EELS. The Ti_2O_3 disordered shell provides two important benefits for enhanced photocatalytic activity. First, as a narrow-band-gap semiconductor, it intrinsically has a high absorption coefficient for solar radiation. Second, as a stoichiometric compound of Ti^{3+}, it is expected to provide a more robust structure than oxygen-deficient rutile for preserving the Ti^{3+} surface species that are the key to the photocatalytic activity of black TiO_2.

METHODS

Sample Preparation. PLV was used as a clean method for synthesizing TiO_2 UNPs by gas phase condensation. By adjusting the density and thermalization dynamics of the laser ablation plume through the choice of laser fluence and background gas pressure, different phases and sizes of TiO_2 nanoparticles could be synthesized. A 2 in. TiO_2 pellet (Praxair Company), composed of rutile powder, was used as ablation target in this experiment. Pulsed KrF (248 nm, 1 J cm^{-2}, 1 Hz) laser vaporization of the targets in room-temperature 200 mTorr O_2 gas was determined for the synthesis conditions in this report to produce a spatially confined laser ablation plasma plume that thermalized over a 5 cm stopping distance and result in the synthesis of UNPs with a diameter of less than 5 nm. The UNPs deposit as loosely assembled aggregates at 5 cm distance from

the target on substrates held at room temperature. Before the deposition process, the target was preablated for 500 pulses to remove the possible contaminants from its surface. The as-synthesized UNPs appeared white on the transparent quartz. After postannealing at 970 ± 20 K for 2 h in Ar gas, the as-deposited UNPs transformed into rutile nanoparticles of dark color. The particle sizes were counted in TEM, and the diameter of more than 90% of NPs was larger than 15 ± 1 nm. Pure Ti_2O_3 nanoparticles were also synthesized by PLV in a He background pressure of 5 Torr. These NPs were used to obtain the standard Ti_2O_3 EELS spectra because they were semicrystalline, similar to the defective Ti_2O_3 structure in the black TiO_2. However, there is no obvious difference of ELNES between the Ti_2O_3 nanoparticles synthesized in our experiments and the commercial Ti_2O_3 particles obtained from Sigma-Aldrich.

Characterization Method. The phase of the TiO_2 nanoparticle's core was determined by high-resolution transmission electron microcopy and nanobeam electron diffraction with a Zeiss Libra 200 MC TEM at an acceleration voltage of 200 kV. The information limit of HRTEM images in this microscope is ∼0.1 nm. The NBED is performed in STEM mode with a 2.5 mrad semiconvergent angle, which is also used to characterize the surface structure of nanoparticles. The electronic structure of TiO_2 nanoparticles was determined by EELS. The energy resolution of EELS with a monochromator is ∼0.15 eV measured at the full width at half-maximum of the zero-loss peak in the vacuum with the highest energy dispersion of 0.025 eV/channel. To obtain the surface structures by directly observing the arrangement of the atoms, we used an aberration-corrected dedicated STEM Nion UltraSTEM 200 to get atomic resolution (57 pm) in the HAADF mode.

Conflict of Interest: The authors declare no competing financial interest.

Supporting Information Available: The Supporting Information is available free of charge on the ACS Publications website at DOI: 10.1021/acsnano.5b04712.

Linear combination of TiO_2–Ti_2O_3 and linear least-squares fit of black rutile from core to shell, detection geometry effect of EELS spectrum on NPs with different sizes, color comparison of nanoparticles synthesized by PLV before and after annealing, calculation of phase diagram for TiO_2–Ti_2O_3 by density functional theory, comparison of EELS spectra taken from crystalline precursor at room temperature and after annealing (PDF)

REFERENCES AND NOTES

1. Chen, X. B.; Mao, S. S. Titanium Dioxide Nanomaterials: Synthesis, Properties, Modifications, and Applications. *Chem. Rev.* **2007**, *107*, 2891–2959.
2. Monticone, S.; Tufeu, R.; Kanaev, A. V.; Scolan, E.; Sanchez, C. Quantum Size Effect in TiO_2 Nanoparticles: Does It Exist? *Appl. Surf. Sci.* **2000**, *162−163*, 565–570.
3. Chen, X. B.; Liu, L.; Yu, P. Y.; Mao, S. S. Increasing Solar Absorption for Photocatalysis with Black Hydrogenated Titanium Dioxide Nanocrystals. *Science* **2011**, *331*, 746–750.
4. Naldoni, A.; Allieta, M.; Santangelo, S.; Marelli, M.; Fabbri, F.; Cappelli, S.; Bianchi, C. L.; Psaro, R.; Dal Santo, V. Effect of Nature and Location of Defects on Bandgap Narrowing in Black TiO_2 Nanoparticles. *J. Am. Chem. Soc.* **2012**, *134*, 7600–7603.
5. Chen, X. B.; Liu, L.; Huang, F. Q. Black Titanium Dioxide (TiO_2) Nanomaterials. *Chem. Soc. Rev.* **2015**, *44*, 1861–1885.
6. Jiang, X. D.; Zhang, Y. P.; Jiang, J.; Rong, Y. S.; Wang, Y. C.; Wu, Y. C.; Pan, C. X. Characterization of Oxygen Vacancy Associates within Hydrogenated TiO_2: A Positron Annihilation Study. *J. Phys. Chem. C* **2012**, *116*, 22619–22624.
7. Stoyanov, E.; Langenhorst, F.; Steinle-Neumann, G. The Effect of Valence State and Site Geometry on Ti $L_{3,2}$ and O K Electron Energy-Loss Spectra of Ti_xO_y Phases. *Am. Mineral.* **2007**, *92*, 577–586.
8. van Aken, P. A.; Liebscher, B.; Styrsa, V. J. Core Level Electron Energy-Loss Spectra of Minerals: Pre-Edge Fine Structures at the Oxygen K-Edge. *Phys. Chem. Miner.* **1998**, *25*, 494–498.
9. Shibata, N.; Goto, A.; Choi, S. Y.; Mizoguchi, T.; Findlay, S. D.; Yamamoto, T.; Ikuhara, Y. Direct Imaging of Reconstructed Atoms on TiO_2 (110) Surfaces. *Science* **2008**, *322*, 570–573.
10. Diebold, U. The Surface Science of Titanium Dioxide. *Surf. Sci. Rep.* **2003**, *48*, 53–229.
11. Onishi, H.; Iwasawa, Y. Reconstruction of TiO_2 (110) Surface: STM Study with Atomic-Scale Resolution. *Surf. Sci.* **1994**, *313*, L783–L789.
12. Onishi, H.; Iwasawa, Y. Dynamic Visualization of a Metal-Oxide-Surface/Gas-Phase Reaction: Time-Resolved Observation by Scanning Tunneling Microscopy at 800 K. *Phys. Rev. Lett.* **1996**, *76*, 791–794.
13. Stone, P.; Bennett, R. A.; Bowker, M. Reactive Re-Oxidation of Reduced TiO_2(110) Surfaces Demonstrated by High Temperature STM Movies. *New J. Phys.* **1999**, *1*, 1.1–1.12.
14. Tominaka, S. Topotactic Reduction Yielding Black Titanium Oxide Nanostructures as Metallic Electronic Conductors. *Inorg. Chem.* **2012**, *51*, 10136–10140.
15. le Roux, H.; Glasser, L. Transferable Potentials for the Ti-O System. *J. Mater. Chem.* **1997**, *7*, 843–851.
16. Van Zandt, L. L.; Honig, J. M.; Goodenough, J. B. Resistivity and Magnetic Order in Ti_2O_3. *J. Appl. Phys.* **1968**, *39*, 594.
17. Dmitrienko, V. E.; Ishida, K.; Kirfel, A.; Ovchinnikova, E. N. Polarization Anisotropy of X-Ray Atomic Factors and 'Forbidden' Resonant Reflections. *Acta Crystallogr., Sect. A: Found. Crystallogr.* **2005**, *61*, 481–493.
18. Nowotny, M. K.; Sheppard, L. R.; Bak, T.; Nowotny, J. Defect Chemistry of Titanium Dioxide. Application of Defect Engineering in Processing of TiO_2-Based Photocatalysts. *J. Phys. Chem. C* **2008**, *112*, 5275–5300.
19. Pan, X. Y.; Yang, M. Q.; Fu, X. Z.; Zhang, N.; Xu, Y. J. Defective TiO_2 with Oxygen Vacancies: Synthesis, Properties and Photocatalytic Applications. *Nanoscale* **2013**, *5*, 3601–3614.